SPHERICAL AIR-BEARING AOCS TESTBED WITH PARASITIC MOMENTS OF INERTIA CANCELLATION

Nemanja Jovanovic[(1)(2)] **and Jaan Praks**[(3)]

[(1)]*Huld Oy, Keilasatama 5, 02150 Espoo, Finland, nemanja.jovanovic@huld.io*
[(2)]*Aalto University, Maarintie 8, 02150 Espoo, Finland, nemanja.jovanovic@aalto.fi*
[(3)]*Aalto University, Maarintie 8, 02150 Espoo, Finland, jaan.praks@aalto.fi*

ABSTRACT

A spherical air-bearing AOCS (Attitude and Orbit Control System) testbed, equipped with an external torque generating subsystem, is proposed. Such a system could enhance satellite hardware testing, verification, and validation capabilities of typical air-bearing testbeds. The externally generated torque can be used for simulating environment disturbance torques, but more importantly it can actively modify and correct the dynamical response of the system under test (SUT). This allows for correction of the SUT's experienced moments of inertia (MOI), or its continuous alteration to simulate complex mechanical processes, such as panel deployment or tether dynamics. This study is focused on the cancellation of the parasitic MOI, which originate from the testbed's spherical enclosure. Capability to remove the parasitic MOI would allow building testbeds for use with flight ready nanosatellites and providing them with nearly realistic dynamic experience, enabling end-to-end validation testing of attitude maneuvre scenarios. The air-bearing testbed is modeled in a numerical simulator. The simulation is used for the development of control algorithms for the parasitic MOI cancelation using external torque generating subsystem. Performance of the testbed and algorithms is characterized and presented.

1 INTRODUCTION

Validation of satellite's attitude determination and control is commonly performed with a number of different tests, which focus on specific aspects, including end-to-end maneuver simulations with hardware-in-the-loop (HIL) setups. These HIL setups vary from simple static testbeds [6], [10], [11], which inject sensor readings and intercept actuator commands, over air-bearing platforms [5], [16], to parabolic flight [1] and free fall tests [8]. Issue with static testbeds is the limiting of the scope of the end-to-end tests by excluding sensors and actuators. Free fall tests, on the other hand, are limited by relatively short test durations.

Air-bearing platforms offer a practical middle ground with possibly unlimited test durations and ability to include the sensors and the actuators of the system under test (SUT) in the end-to-end simulations. Despite these benefits of air-bearing platforms, they unavoidably alter the physical properties relevant to the tests and this lead to inaccurate results. The alteration mainly comes as the increased moments of inertia (MOI) after the SUT's body is affixed to the testbed. In some cases, reduction of the MOI can happen as well, when the platform can not support mounting the complete satellite body. The discrepancy between the MOI of the satellite (in-flight) and the actual MOI of the SUT after affixing to the testbed is termed the parasitic MOI in this article. Additionally, the center of mass and the center of rotation of the SUT may be altered, although this is problematic only in certain cases.

This article explores the possibility to provide SUT with the experience of the MOI similar to the expected in flight. The experienced MOI can be changed through continuous application of correcting torques on the testbed, which would enable cancellation of the parasitic MOI. This is done by equipping the testbed with a torque generating subsystem and a sufficiently accurate angular velocity tracking. Uses of such system can be broader and include simulation of the environmental torques and scenarios with complex dynamics (e.g. tether dynamics, panel deployment, beam vibrations, fuel sloshing), as well as for automated MOI measurements of the SUT. However, in this article, the focus is only on the parasitic MOI cancellation.

There are numerous design options to consider when building such a testbed. The design choices can also differ depending on the size and type of the SUT. For the nanosatellite class, ranging from $1\,\mathrm{kg}$ to $10\,\mathrm{kg}$ of mass, it is possible to house them inside a spherical enclosure, which acts as the rotational part of the air-bearing platform. This air-bearing type allows for unconstrained rotational freedom. Additionally, it permits aligning the center of rotation with the SUT's center of mass. Manufacturing spherical enclosure for larger satellites is difficult, due to the need to maintain rigidity and surface evenness. Moreover, the enclosure's MOI, in general, increases faster than the MOI of a SUT with the size of the setup, posing further problems with the setup's sensitivity, as the effects of the SUT torques get significantly attenuated. Thus, for the larger satellites, often the table-top air-bearing configuration with smaller half-sphere rotational element is preferred, sacrificing the rotational freedom and coincidence of SUT's center of mass with the center of rotation for lower parasitic MOI and air-bearing platform's rigidity. The choice of the air-bearing platform type also determines the type of the subsystem for generation of the correction torques. Spherical enclosure permits the use of external subsystems, acting from the static part of the platform on the enclosure's surface. With external subsystems, the torque production can be unlimited and the angular momentum is also externally exchanged, avoiding the issues with actuator saturation. On the other hand, the table-top platforms are generally constrained to internal subsystems, fixed to the rotational part of the platform, contributing to the increase of the parasitic MOI.

Main focus of the research on the air-bearing testbeds is with weight balancing methods [15] for cancelling the unwanted torques arising from displacement of the center of the rotation from the center of the mass. Furthermore, when a testbed platform is equipped with torque generation subsystem, it is most commonly of the internal type. The platforms are intended to be self sufficient and directly used, instead of the SUTs, for development and validation of the attitude control algorithms. While testbeds with spherical enclosures are gaining popularity for use with nanosatellites [13], [14], still the majority of the testbeds are designed with the table-top configuration. The authors of this article are not aware of any other platform with a design and capabilities comparable to the testbed proposed here, a platform with spherical enclosure and an external torque generation subsystem, which is able to provide nearly realistic dynamical response for SUTs as they would experience during the mission. Still, further design parameters and choices have to be identified. Most notably the required torque strength and the torque controllability of the actuators. Equally important is the performance of the attitude and angular velocity tracking sensors. A numerical simulator is developed to help determine the needed actuator and sensor parameters, and to better understand the impact of design choices regarding different air-bearing platform sizes and attitude manuever scenarios.

The article first describes the testbed modelling and designs and the necessary theory is explained. The control laws for the parasitic MOI cancellation are then explained, followed by the description of the developed simulator to evaluate the feasibility of the testbed. Then three different maneuver scenarios and four different SUTs are specified for the evaluation of the control laws. Finally the obtained results are presented and a conclusion is given with further steps identified.

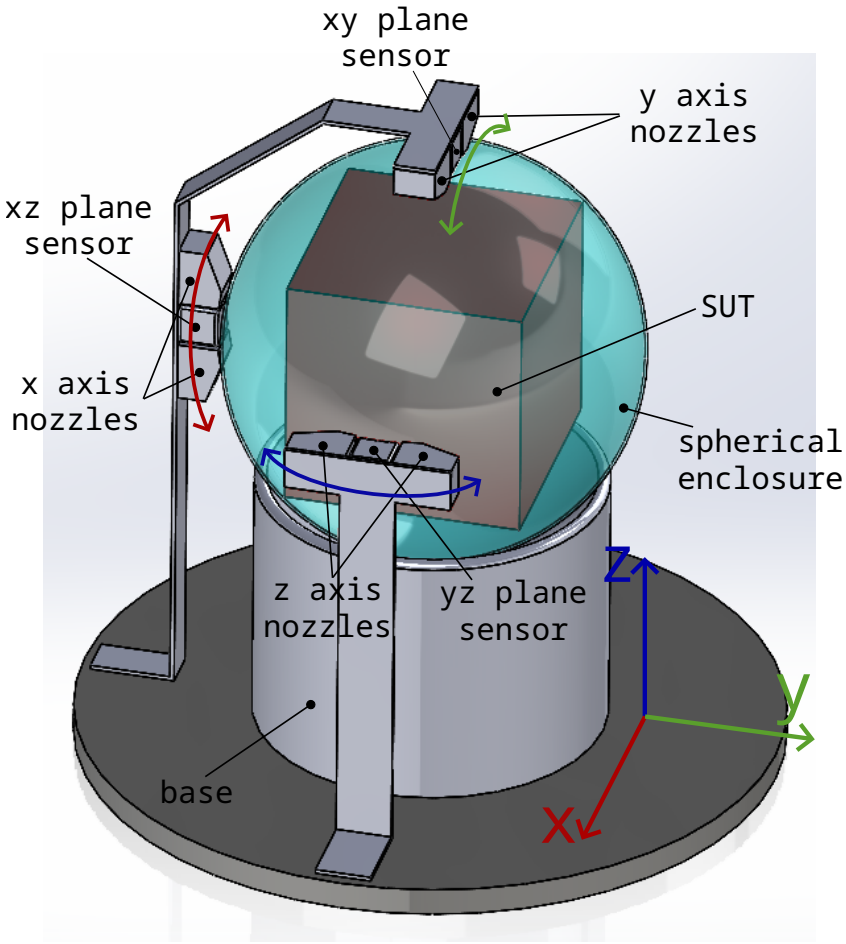

Figure 1: Conceptual design of the proposed air-bearing testbed.

2 TESTBED DESIGN

A conceptual design of the proposed testbed is shown in the Fig. 1. It will consist of the air-bearing platform, with a static base which have a concave socket and a freely rotating spherical enclosure which would house the SUT. The air-bearing platform would be supplemented with an external subsystem for torque generation, containing at least 6 nozzles for thrusting pressurized air. Two nozzles per each of X, Y and Z rotation axes are needed for generating torques of the opposite directions. The attitude and angular velocity tracking subsystem is also equipped with surface motion sensors. Three sensors, for XY, XZ and YZ planes, are depicted. A computational unit is needed to determine the torques exerted by the SUT, and to calculate and command the compensation torques to alter the rotary motion of the spherical enclosure.
Two frames of reference are of interest for the testbed. First is the inertial frame fixed with the testbeds base, and second is the frame fixed to the SUT's body, with the frame axes aligned with the principal axes of the SUT.

2.1 Air-bearing platform base

The main design choices for the stator of the air-bearing platform are the socket size and placement of the grooves and orifices for the distribution of the pressurized air and thin air film creation between the base and the spherical enclosure. Alternatively, a highly porous material can be used for the socket. The socket design influences the load capacity and stiffness of the air-bearing platform. However,

these parameters and design choices are not relevant for the simulation and are not modeled.

2.2 Spherical enclosure

Spherical enclosure should be rigid enough to prevent in-operation deviations of its MOI and the center of mass, but also optimized for low contribution to the parasitic MOI. Furthermore, air-bearing testbeds are often used together with a Helmholtz coil to simulate the Earth orbit environment. Thus, the material used for the enclosure needs to be highly transparent for environmental magnetic field, have sufficient rigidity, low density, but also to be easily moldable or machinable into the spherical shape. There are several candidate types of plastics and the selection should be further informed by the design of the internal support structure and manufacturing capabilities. For simplicity, it is assumed that the acrylic plastic material is used with a density of $1.18\,\mathrm{g\,cm^{-1}}$.
The main design parameter of the spherical enclosure is it's radius, which determines the size of the supported SUT and the amount of parasitic MOI it contributes. Two spherical enclosure with different radiuses will be used in this study's simulations, $200\,\mathrm{mm}$ and $300\,\mathrm{mm}$. Assuming the enclosure thickness of $5\,\mathrm{mm}$ and $10\,\mathrm{mm}$, respectively and using the Eq. 1 for calculation of the spherical shell MOI

$$I = \frac{8\pi}{15}\rho({r_2}^5 - {r_1}^5), \tag{1}$$

where ρ is the material density, r_2 is the outer radius and r_1 is the inner radius, the approximated principal MOI for the enclosures are $0.085\,\mathrm{kg\,m^2}$ and $0.750\,\mathrm{kg\,m^2}$.

2.3 Torque generation subsystem

Torque will be generated by exerting pressurized air through a nozzle on the outer surface of the spherical enclosure angled in a direction the momentum should be impacted. The force impacted by a single nozzle can be approximated with the drag equation (Eq.2)

$$\vec{F_d} = \frac{1}{2}\rho C_d A \vec{v}^2, \tag{2}$$

where ρ is the air density, A is the affected area, C_d is the area's drag coefficient and $\vec{v}$ the average velocity of the exerted air. If $\vec{r}_A$ is a vector from the center of rotation to the center of the area A, the torque generated by the drag force is as in Eq. 3.

$$\vec{\tau}_n = \vec{r}_A \times \vec{F_d} \tag{3}$$

Eq. 2 and Eq. 3 indicate that the torque is proportional with the nozzle area, pressure of the air source and the radius of the enclosure. However, determining individual parameter values in Eq. 2 is laborious and complex due to vagueness of the impacted area, air velocity spread and unknown drag coefficient.
The air supply to the nozzles can be controlled using a solenoid flow control valve. With precise control of flow rate, the nozzle torque can be precisely controlled as well, for a constant air pressure at the source. However, the valves usually have settling time before the desired flow rate is reached, and often it differs for opening and closing [2], [4]. Here the nozzle torques are modeled with symmetrical settling time, as in Eq. 4,

$$\vec{\tau}_n = (\tanh(kt_c)(Q - Q_{prev}) + Q_{prev})C_f \vec{r}_A \times \hat{n}, \tag{4}$$

where Q and Q_{prev} are currently commanded and previously applied flow rates, C_f is a flow rate to drag force conversion coefficient, t_c is elapsed time since the last flow rate command, k is a settling

time coefficient and $\hat{n}$ is a unit vector of a drag force direction. C_f conversion constant can be experimentally measured to precisely model the torque generation. However, for simplicity in the simulations in this article a value $C_f = 1$ is assumed. Settling time coefficient was set to $k = 325$, with which the flow reaches $99.7\,\%$ of the commanded flow rate in $10\,\mathrm{ms}$, and the value has notable effects in the simulations, with the aim of checking whether the effects are problematic for the desired torque application.
To have the capability to generate torque in all directions, at least six nozzles are required, two per a rotational axis, pointing in opposite directions. Additional nozzles can be added for every axis, if there is sufficient surface space, to increase the maximum appliable torque.

2.4 Attitude and angular velocity tracking subsystem

Accurate and prompt tracking of the attitude and angular velocity of the air-bearing platform is crucial for proper cancellation of the parasitic MOI. The attitude change and angular velocity can be measured using laser or optical mouse navigation sensors. A single sensor is able to track only two axes of motion, in the plane tangential to the enclosure's surface at the sensors location. Therefore, at least two sensors are needed to have a full tracking capability. For symmetry and improved tracking accuracy, three sensors can be used so that each of the three axes of motions are tracked by two sensors simultaneously. The value that the sensor provides is the distance traveled by the sensed surface in X and Y sensor directions since the last reading. If Δx_k and Δy_k designate the values read by the sensor k, which is located at the position $\vec{r}_k$ and it's X and Y reading directions are designated with $\hat{s}_{kx}$ and $\hat{s}_{ky}$ unit vectors, and the change of rotation is given with the Euler vector $\vec{\theta}$, then the distance traveled reported by the sensor is obtained as in Eq. 5. The $\vec{\sigma}_{noise}$ is the noise of the sensor.

$$\begin{bmatrix}\Delta x_k \\ \Delta y_k\end{bmatrix} = \begin{bmatrix}\hat{s}_{kx}^T \\ \hat{s}_{ky}^T\end{bmatrix} (\vec{\theta} \times \vec{r}_k) + \vec{\sigma}_{noise} \tag{5}$$

Combining the readouts of K sensors and recovering the change of rotation Euler vector $\vec{\theta}_s$ is then obtained as in Eq. 6

$$\vec{\theta}_s = diag(\sum_{k\in 1..K} (|\vec{r}_k \times \hat{s}_{kx}|_{xyz} + |\vec{r}_k \times \hat{s}_{ky}|_{xyz}))^{-1} \sum_{k\in 1..K} (\Delta x_k \vec{r}_k \times \hat{s}_{kx} + \Delta y_k \vec{r}_k \times \hat{s}_{ky}), \tag{6}$$

where $|\vec{v}|_{xyz}$ is operation which makes all vector components positive. Angular velocity is then obtained by dividing the Euler vector $\vec{\theta}_s$ by the time elapsed since the last sensors readout Δt_s,

$$\vec{\omega}_s = \frac{\vec{\theta}_s}{\Delta t_s}. \tag{7}$$

The attitude and angular velocity tracking subsystem for this study was modeled with three sensors positioned along each of the testbed's reference frame axes. X and Y axes of each sensor is then aligned parallel with the other two axes of the testbed's reference frame. For different sensor configurations, [9] provides information on calculation of the optimal weights for the sensor values.
The attitude is tracked by converting the Euler vector to the unit quaternion representation and premultiplying with the last testbed attitude, q_{tb}, each time the new reading is available, as given in the Eq. 8.

$$q_{tb} = \begin{bmatrix}\cos(\frac{|\vec{\theta}_s|}{2}) \\ \sin(\frac{|\vec{\theta}_s|}{2}) \frac{\vec{\theta}_s}{|\vec{\theta}_s|}\end{bmatrix} \circ q_{tb_{prev}} \tag{8}$$

For modelling of the angular position tracking, the ADNS-6010 [7] sensor was used as a reference, with 2000 cpi (counts per inch) resolution and frame rate of up to 7080 fps (frames per second).

Applied to the two spherical enclosures with radiuses of $200\,\mathrm{mm}$ and $300\,\mathrm{mm}$, maximal measurable angular velocities are $5.71\,\mathrm{rad\,s^{-1}}$ and $3.81\,\mathrm{rad\,s^{-1}}$, with minimal measurable steps of $6.35\,\mu\mathrm{rad\,s^{-1}}$ and $4.23\,\mu\mathrm{rad\,s^{-1}}$, respectively. However, the two most significant parameters for testbed performance are the average measurement error and the highest possible data polling frequency. The average measurement error can be estimated from the plot provided in the sensors's datasheet document which showcases maximum distance measurement errors for different lens distances from the navigation surface and different surface types. Nominally, the error stays under $0.2\,\%$. As the surface properties of the spherical enclosure are not known, and the sensed area will be slightly curved, additional margin is applied and the used average measurement error in the simulations is $0.25\,\%$. The data readout frequency maximums are around $10\,\mathrm{kHz}$ and $50\,\mathrm{kHz}$ for passive and active line drive modes. The simulations assume $500\,\mathrm{Hz}$ polling rate, which is well under the limits for the sensor.
In general, as the mouse navigation sensors are providing relative measurements, it can be expected that position tracking error will accrue over time. The error originates from sensor's internal manufacturing inaccuracies, errors in sensor alignments in the testbed setup and sensing resolution limitation. Absolute position tracking method is therefore necessary to eliminate the errors. This can be done by placing different markings with discernable orientation on the enclosure and using a camera to track the markings. Processing the camera images is slow, so the angular position corrections are to be expected with frequency of around $1\,\mathrm{Hz}$. However, for the purposes of this article, the sensor positioning is assumed ideal and sensor output biases corrected. While the noise of the sensor is still modeled, the simulation durations are short enough that integration errors are small and modeling the absolute position tracking is not necessary.

3 PARASITIC MOMENTS OF INERTIA CANCELLATION CONTROL LAWS

Two control laws were considered for cancellation of the parasitic MOI. First control law is direct torque compensation, calculated from the currently sensed angular velocity and determined torque produced by the SUT, while the second is a Proportional Integral Derivative (PID) controller on the error state between the current angular velocity and the expected angular velocity of the SUT. However, the direct control law proved to be usable only with high frequency control loops and was significantly sensitive to the measurement noise. Because it performed poorly for the conditions assumed to be realistic in this study, the simulation results of this control law are not presented. Still, this control law is based on the exact torque compensation, and it can be useful for designing other more robust control laws, so it's derivation is still shown.
As the knowledge of the torque produced by the SUT is necessary for both control laws, its determination is explained first. For every time step n (with previous time step denoted with $n-1$), the expected angular velocity of the testbed $\vec{\omega}_{exp_n}$ is calculated by integrating Euler's rotation equation for the testbed, Eq. 9, and assuming the SUT is not exerting any torque. For the integration the Runge-Kutta method (canonical 4th order version) is used.

$$\vec{\omega}_{exp_n} = \vec{\omega}_{s_{n-1}} + \int_{t_{n-1}}^{t_n} I_{tot}^{-1}(\vec{\omega}_{s_{n-1}} \times I_{tot}\vec{\omega}_{s_{n-1}} - \vec{\tau}_{tb_{n-1}})\delta t \tag{9}$$

In Eq. 9, $I_{tot} = I_{sut} + I_{se}$, is a combined moments of inertia of both SUT and the spherical enclosure, $\vec{\tau}_{tb_{n-1}}$ is the torque produced by the testbed in the previous time step and $\vec{\omega}_{s_{n-1}}$ is the angular velocity sensed by the attitude and angular velocity subsystem at the time of the previous time step.
Then, from the difference of the calculated expected angular velocity and the angular velocity sensed at the time of the current time step, the SUT torque is obtained with Eq. 10,

$$\vec{\tau}_{sut} = I_{tot}\frac{\vec{\omega}_{exp_n} - \vec{\omega}_{s_n}}{\Delta t_{tb}}, \tag{10}$$

where $\Delta t_{tb} = t_n - t_{n-1}$ is time difference between two consecutive steps.

3.1 Direct control law

Euler's rotation equation for the SUT only, without the spherical enclosure, is as in Eq. 11

$$I_{sut}\dot{\vec{\omega}}_{s_n} = \vec{\omega}_{s_n} \times I_{sut}\vec{\omega}_{s_n} - \vec{\tau}_{sut}, \tag{11}$$

while Euler's rotation equation for the SUT on the testbed is as in Eq. 12, with the testbed generated torque $\vec{\tau}_{tb}$.

$$I_{tot}\dot{\vec{\omega}}_{s_n} = \vec{\omega}_{s_n} \times I_{tot}\vec{\omega}_{s_n} - \vec{\tau}_{sut} - \vec{\tau}_{tb} \tag{12}$$

By solving the Eq. 11 for $\dot{\vec{\omega}}_{s_n}$, inserting it into Eq. 12 and then solving for $\vec{\tau}_{tb}$ provides the compensation torque to be generated by the testbed, as shown in Eq. 13.

$$\vec{\tau}_{tb} = \vec{\omega} \times I_{tot}\vec{\omega} - I_{tot}I_{sut}^{-1}(\vec{\omega} \times I_{sut}\vec{\omega}) + (I_{tot}I_{sut}^{-1} - diag(1,1,1))\vec{\tau}_{sut} \tag{13}$$

3.2 Proportional Integral Derivative control law

PID control law is acting on the angular velocity error $\vec{\omega}_{err}$, which is obtained by integrating the Euler rotation equation Eq. 14 to obtain the expected angular velocity of the SUT, with the real SUT's MOI, using the Runge-Kutta method. This integration is repeated each time step n, to continuously track the evolution of the SUT's expected dynamics. Initial angular velocity $\vec{\omega}_{sut_0}$ is equal to the angular velocity of the spherical enclosure at the start of the control.

$$\vec{\omega}_{sut_n} = \vec{\omega}_{sut_{n-1}} + \int_{t_{n-1}}^{t_n} I_{sut}^{-1}(\vec{\omega}_{sut_{n-1}} \times I_{sut}\vec{\omega}_{sut_{n-1}} - \vec{\tau}_{sut})\delta t \tag{14}$$

Then, the difference between the sensed angular velocity of the spherical enclosure $\vec{\omega}_{s_n}$ and the expected SUT angular velocity $\vec{\omega}_{sut_n}$ (Eq. 15) can be used in the control law given in Eq. 16, with K_P, K_I and K_D being proportional, integrational and differential coefficients.

$$\vec{\omega}_{err} = \vec{\omega}_{s_n} - \vec{\omega}_{sut_n} \tag{15}$$

$$\vec{\tau}_{tb_n} = K_P\vec{\omega}_{err} + K_I\sum_{k=0}^{n}\vec{\omega}_{err_k} + K_D(\vec{\omega}_{err_n} - \vec{\omega}_{err_{n-1}}) \tag{16}$$

The calculated testbed torque $\vec{\tau}_{tb_n}$ is in the frame of reference of the SUT, and should be transformed to the testbeds inertial frame of reference before it is exerted by the torque generating subsystem, which can be done using the attitude tracked with Eq. 8. Additional care needs to be taken for implementing the Runge-Kutta method to account for the orientation change of $\vec{\tau}_{tb_{n-1}}$ in the previous Δt time step. Also, as there is a delay before the new calculated torque is applied and because there is a settling time from the Eq. 4, the precision can be improved by performing the integration of Eq. 9 in two steps, first with torque $\vec{\tau}_{tb_{n-2}}$ and then with $\vec{\tau}_{tb_{n-1}}$. Similarly, the sensed angular velocity $\vec{\omega}_{s_n}$ is available in the testbed's frame of reference and should be transformed to the frame of reference of the SUT before calculating the SUT's torque and angular velocity error.

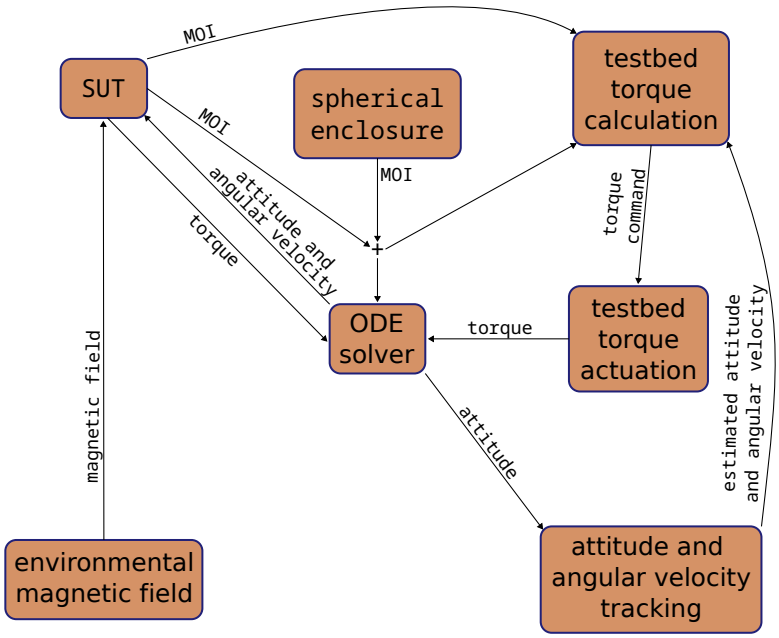

Figure 2: Simulation block diagram with data exchange.

4 SIMULATION

The simulation for the testbed was developed in the Julia programming language, using the DifferentialEquations.jl library package [12] which provides efficient solvers for a various types of differential equations. This simulation models the testbed dynamics with Euler's rotation equation and tracks the attitude with unit quaternions, as given in the Eq. 17. The Ordinary Differential Equation (ODE) solver DP8 (Hairer's 8/5/3 adaption of the Dormand-Prince Runge-Kutta method [3]) was used for the integration.

$$\dot{q} = \begin{bmatrix} 0 & -\omega_x & -\omega_y & -\omega_z \\ \omega_x & 0 & \omega_z & -\omega_y \\ \omega_y & -\omega_z & 0 & \omega_x \\ \omega_z & \omega_y & -\omega_x & 0 \end{bmatrix} q \tag{17}$$
$$\dot{\vec{\omega}} = I^{-1}(\vec{\omega} \times I\vec{\omega} - \vec{\tau}_{tb} - \vec{\tau}_{sut})$$

In Fig. 2, a block diagram of the simulator is provided, with data exchanged between the blocks shown. The ODE solver, with the ODE equations from Eq. 17 takes as the inputs the total MOI as the sum of the MOIs of the SUT and the spherical enclosure, as well as the torque values produced by the SUT and the testbed. The solver produces the true attitude and angular velocity values. The SUT takes the output from the solver, and depending on the maneuver and the actuator types can take as the input the environmental magnetic field and produce the torque. The attitude and angular velocity tracking block takes the true attitude from the ODE solver and calculates the estimates of attitude and angular velocity as described in the section 2.4. The testbed torque actuation block, using the model from section 2.3, generates the torque after receiving the torque command from the testbed torque calculation block. Lastly, the torque calculation block takes as the inputs the MOI of the SUT and the sum of the SUT's and spherical enclosure's MOIs, as well as the estimated attitude and angular velocities to produce the torque command for the testbed torque actuation block.
The DifferentialEquations.jl package also allows injection of callbacks at desired times during the

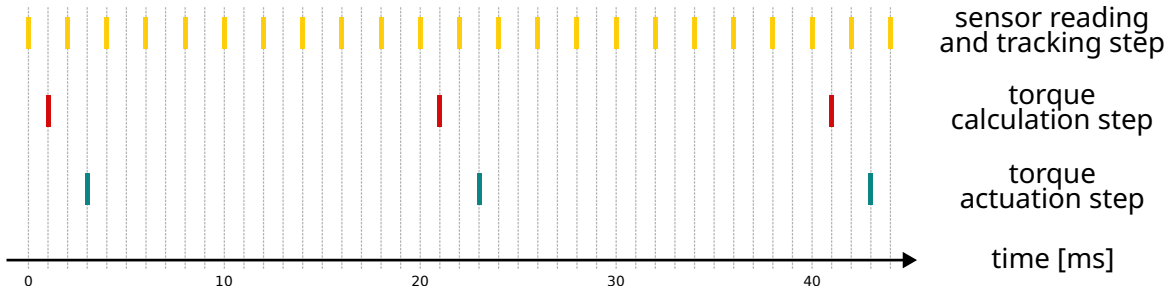

Figure 3: Timeline of the simulated execution steps testbed components.

solving process. This was used to model the execution of attitude and angular velocity tracking, with frequency of $500\,\mathrm{Hz}$, matching the selected polling frequency of the mouse navigation sensors, and the execution of the testbed controller and torque actuation, with frequency of $50\,\mathrm{Hz}$ where torque actuation is executed $2\,\mathrm{ms}$ after the execution of the testbed controller step. The timing diagram is shown in the Fig. 3. The torque production of the SUT is updated with frequency of $1\,\mathrm{Hz}$.

5 MANEUVER SCENARIOS

Three different maneuver scenarios will be used for simulating and evaluation of the parasitic MOI cancellation performance of the air-bearing testbed:

Passive SUT No torque is generated by the SUT and it starts with initial angular velocity of $\vec{\omega}_0 = [0.5, 0.5, 0.5]\mathrm{rad\,s^{-1}}$.

Pointing maneuver Starting from a motionless state $\vec{\omega}_0 = [0, 0, 0]\mathrm{rad\,s^{-1}}$, the SUT performs three rotation steps of $90°$ around its body's X, Y and Z axes consecutively and then returns to the original position. Every step is provided with $1\,\mathrm{min}$ of time to be performed. The pointing controller in this scenario updates the output torque with the frequency of $5\,\mathrm{Hz}$.

Detumble Using magnetorquer actuators and B-dot control law, SUT lowers the initial angular velocity $\vec{\omega}_0 = [0.5, 0.5, 0.5]\mathrm{rad\,s^{-1}}$. Static environmental magnetic field of $40\,\mathrm{nT}$ is assumed. The detumbling controller in this scenario updates the output magnetic moment with the frequency of $5\,\mathrm{Hz}$.

Each maneuver is simulated for $4\,\mathrm{min}$. The manuever simulations will be performed with three different SUT cases. Each SUT is modeled with reaction wheels, magnetorquers and magnetometer so they can be used in each of the four scenarios. The SUTs are:

1U CubeSat Principal MOI is estimated from a uniform cube of dimensions $10\,\mathrm{cm} \times 10\,\mathrm{cm} \times 10\,\mathrm{cm}$ and mass of $1.33\,\mathrm{kg}$, giving $[0.00221, 0.0222, 0.0223]\mathrm{kg\,m^2}$. This SUT is used with the smaller spherical enclosure. The testbed's PID controller coefficients were set to $K_P = 2.5 \times 10^{-1}$, $K_I = 1 \times 10^{-4}$ and $K_D = 5 \times 10^{-4}$.

3U CubeSat Principal MOI is estimated from a rectangular cuboid of dimensions $10\,\mathrm{cm} \times 10\,\mathrm{cm} \times 30\,\mathrm{cm}$ and mass of $3\,\mathrm{kg}$, giving $[0.005, 0.025, 0.0251]\mathrm{kg\,m^2}$. This SUT is used with the smaller spherical enclosure. The testbed's PID controller coefficients were set to $K_P = 5 \times 10^{-1}$, $K_I = 3 \times 10^{-3}$ and $K_D = 1 \times 10^{-2}$.

Microsatellite AOCS A microsatellite is too large to fit in the larger spherical enclosure, so only its AOCS (Attitude and Orbit Control System) is placed in the testbed. The principal MOI of the AOCS is assumed to be $[0.08, 0.08, 0.08]\mathrm{kg\,m^2}$. The principal MOI of the microsatellite is assumed to equal $[1.525, 2.225, 2.5]\mathrm{kg\,m^2}$. This SUT is used with the larger spherical enclosure. With this SUT, contrary to previous SUTs, the testbed adds instead of removing the apparent MOI. The testbed's PID controller coefficients were set to $K_P = 2.5 \times 10^1$, $K_I = 0$ and $K_D = 0$.

6 RESULTS

For each described SUT and maneuver, a plot of the angular velocity vector evolution is provided with the three vector components in the SUT's body frame of reference given separately, in Figures 4 to 12. Three different simulation runs are overlaid: the run showing the angular velocity evolution of the SUT without the spherical enclosure and without the parasitic MOI cancellation torque actuation (reference), the run with the spherical enclosure and without the parasitic MOI cancellation torque actuation (cancellation off), and the run with both the spherical enclosure and parasitic MOI cancellation torque actuation (cancellation on). The reference run is provided to establish the desired behavior, while the run without the cancellation torque shows the effects of the added MOI when the SUT is affixed to the spherical enclosure.

Figure 4 shows the passive scenario simulation with the 1U CubeSat SUT. While the spherical enclosure has its principal MOI components equal, they are nearly equal for the SUT. Because of this, the angular velocity vector in the case of the reference run is changing relatively little, while with the addition of the spherical enclosure the change is barely visible. Still, the difference between those two runs is notable on the plot. The run with the parasitic MOI cancellation torque applied shows that the dynamical response is corrected and the angular velocity vector follows the reference run. However, some noise is added to the dynamical response.

Figure 5 shows the pointing maneuver scenario simulation with the 1U CubeSat SUT. The difference between the reference run and the run without the parasitic MOI cancellation is significant. The SUT is not able to complete any of the pointing maneuver steps in time with the added MOI. However, with the parasitic MOI cancellation torque applied, the SUT's angular velocity vector closely follows the plot of the reference run.

Figure 6 shows the detumble scenario simulation with the 1U CubeSat SUT. The difference between the reference run and the run without the parasitic MOI cancellation is quite notable. The detumbling rate of the SUT with added MOI is slowed down. When the parasitic MOI cancellation torque is applied, the SUT's angular velocity vector evolution mirrors the plot of the reference run with a small offset and some noise added.

Figure 7 shows the passive scenario simulation with the 3U CubeSat SUT. With one SUT's principal MOI five times smaller than the other two, the change of the angular velocity components is apparent in the plot. The addition of the parasitic MOI significantly slows down its change rate. When the parasitic MOI cancellation torque is applied, the angular velocity vector evolution is very similar to the reference run. However, some noise is noticeable on the X axis component, where the range of the change is relatively small.

Figure 8 shows the pointing maneuver scenario simulation with the 3U CubeSat SUT. The difference between the reference run and the run without the parasitic MOI cancellation is significant. The SUT is not able to complete any of the pointing maneuver steps in time with the added MOI. However, with the parasitic MOI cancellation torque applied, the SUT's angular velocity vector closely follows the plot of the reference run.

Figure 9 shows the detumble scenario simulation with the 3U CubeSat SUT. The difference between

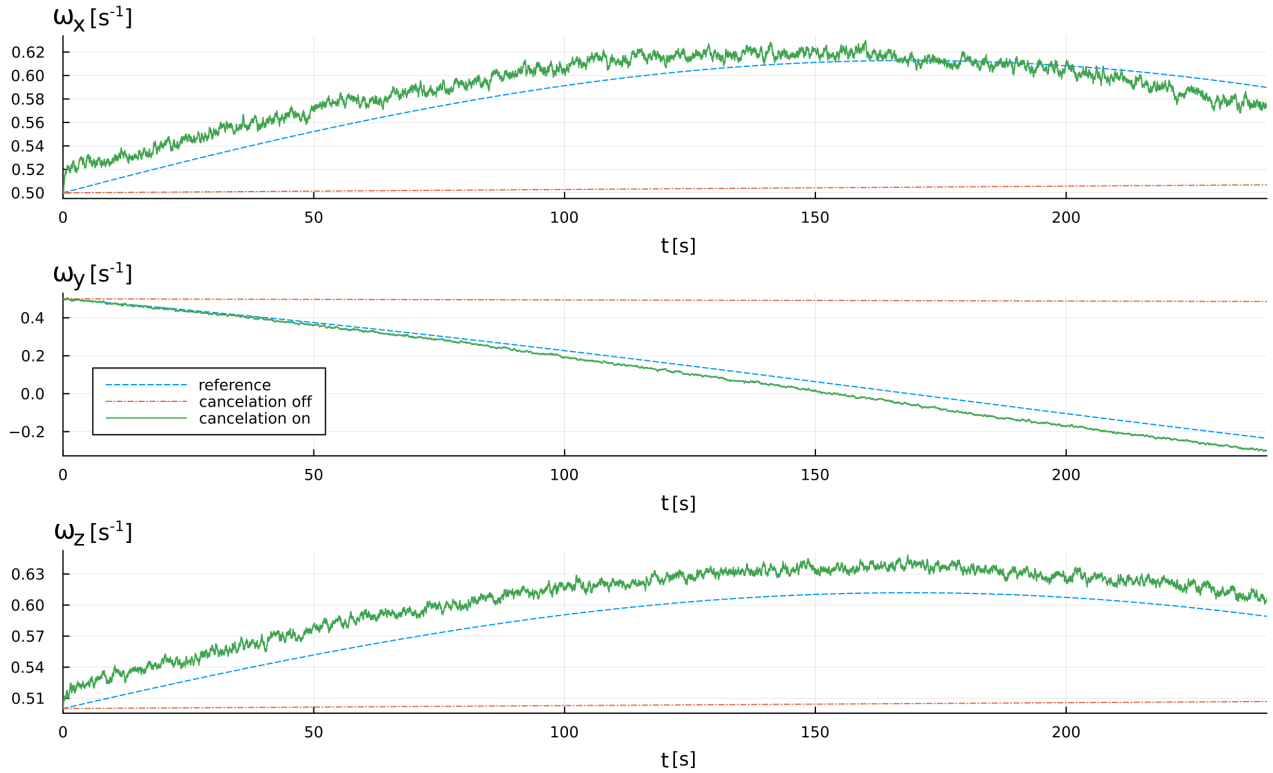

Figure 4: Angular velocity plot of the passive scenario simulation with 1U CubeSat SUT.

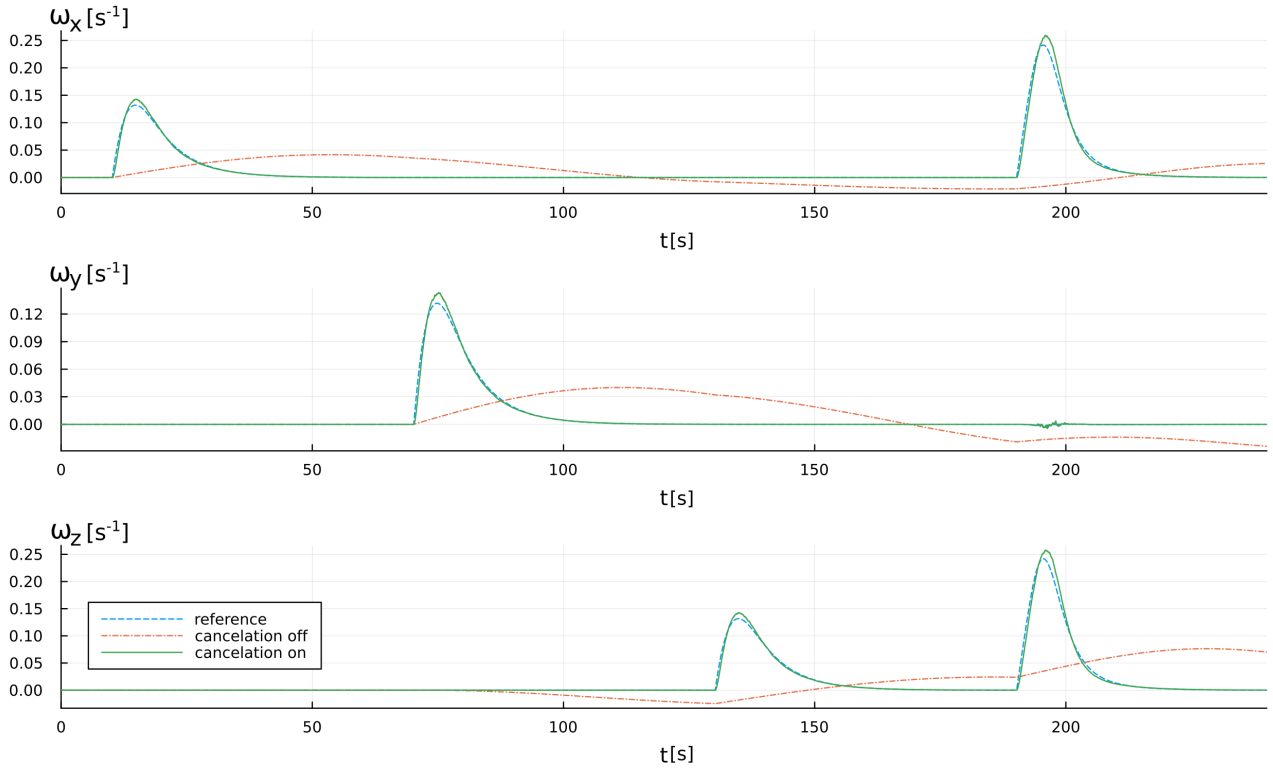

Figure 5: Angular velocity plot of the pointing maneuver scenario simulation with 1U CubeSat SUT.

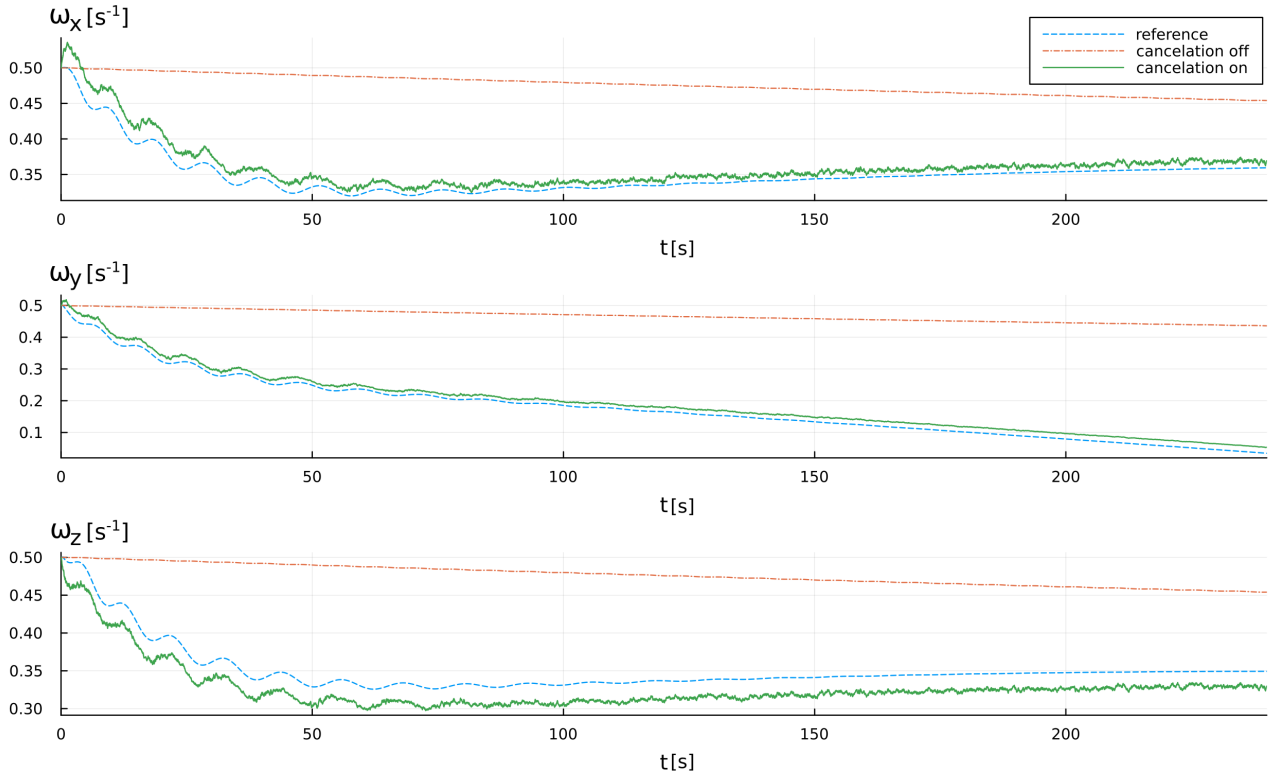

Figure 6: Angular velocity plot of the detumble scenario simulation with 1U CubeSat SUT.

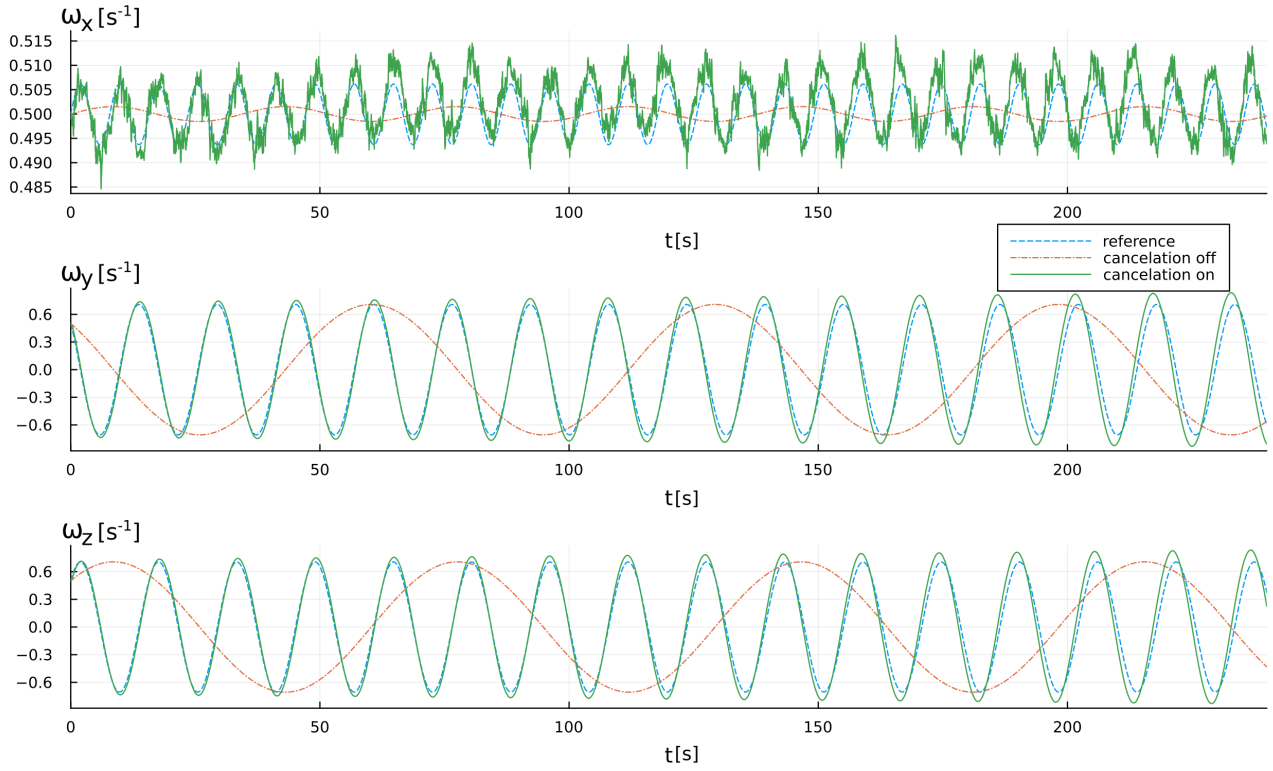

Figure 7: Angular velocity plot of the passive scenario simulation with 3U CubeSat SUT.

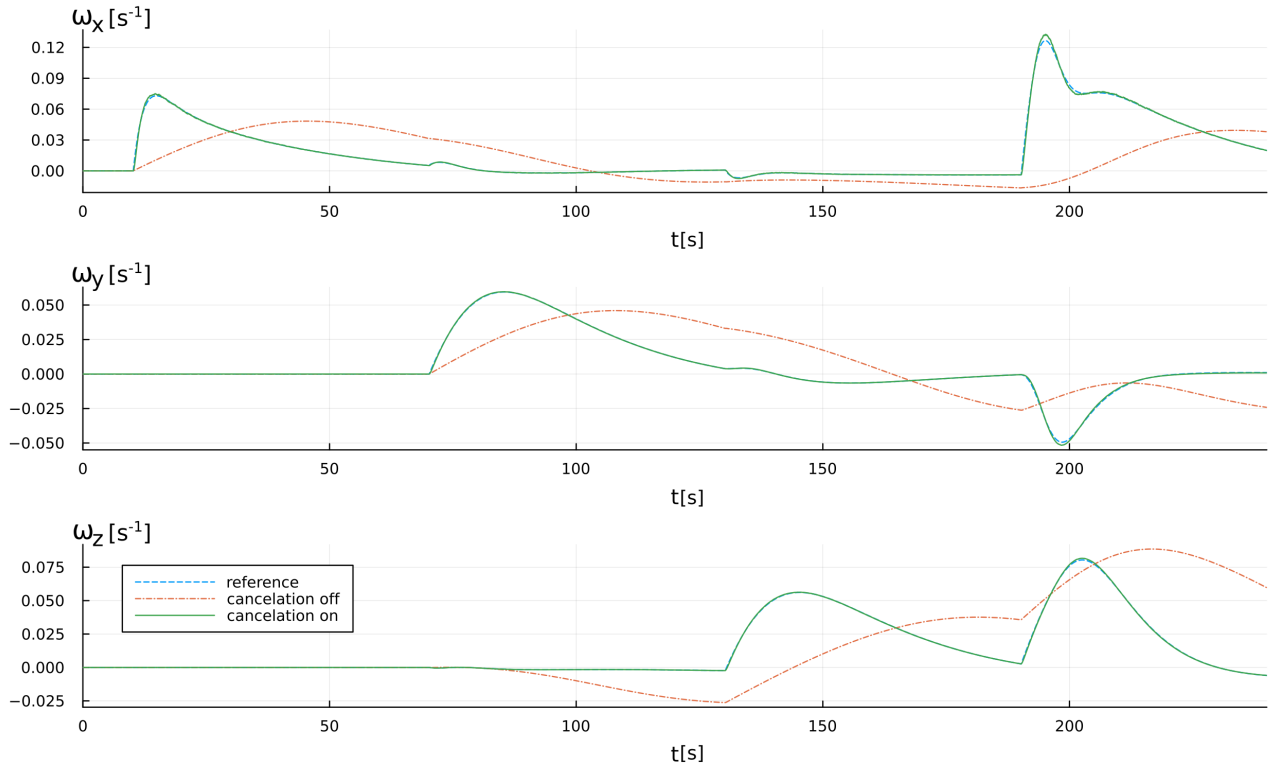

Figure 8: Angular velocity plot of the pointing maneuver scenario simulation with 3U CubeSat SUT.

the reference run and the run without the parasitic MOI cancellation is quite notable. While the reference run successfully detumbles Y and Z components of the angular velocity and to some extent increases the X component, in the case with the added parasitic MOI all the components are detumbled slightly and nearly equally. The parasitic MOI cancellation torque manages to make the angular velocity resemble the dynamical response in the reference run, although some deviation is present.

Figure 10 shows passive scenario simulation with the microsatellite AOCS SUT. The microsatellite has the MOI components that mutually differ sufficiently to make the reference run with different evolutions of all three angular velocity components. On the other hand, the AOCS and the spherical enclosure have their principal MOI components equal, and the simulation run without the parasitic MOI cancellation torque has the constant angular velocity vector. When the parasitic MOI cancellation torque is applied, the angular velocity closely mirrors the reference run.

Figure 11 shows the pointing maneuver scenario simulation with the microsatellite AOCS SUT. This case has the reference run and the run without the parasitic MOI cancellation with similar, but still noticeable difference. The reference simulation run is with slightly slower dynamics and lower peaks of the angular velocity vector. Addition of the parasitic MOI cancellation torque successfully corrects this difference.

Figure 12 shows the detumble scenario simulation with the microsatellite AOCS SUT. The difference between the reference run and the run without the parasitic MOI cancellation is significant. While the reference run successfully detumbles Y and Z components of the angular velocity and to some extent increases the X component, in the case with the added parasitic MOI only the X component is significantly detumbled. The parasitic MOI cancellation torque manages to make the angular velocity mirror the dynamical response in the reference run very closely.

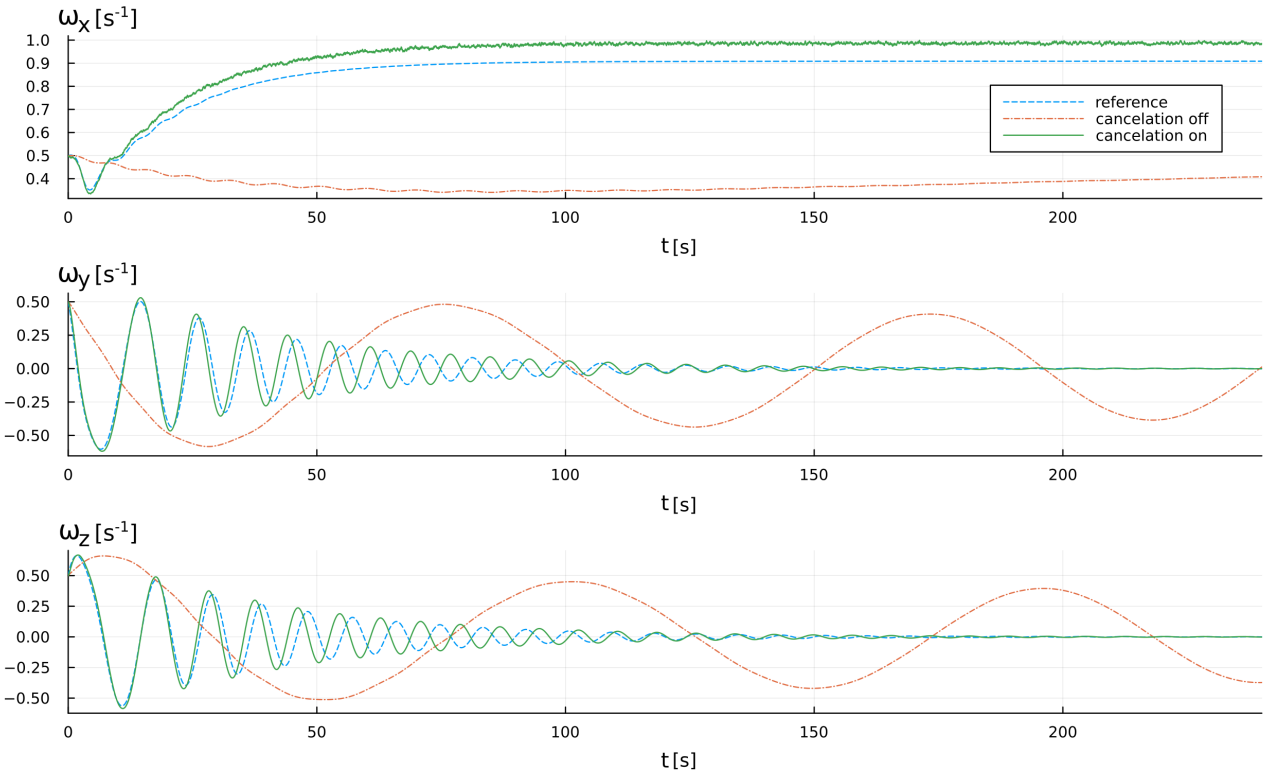

Figure 9: Angular velocity plot of the detumble scenario simulation with 3U CubeSat SUT.

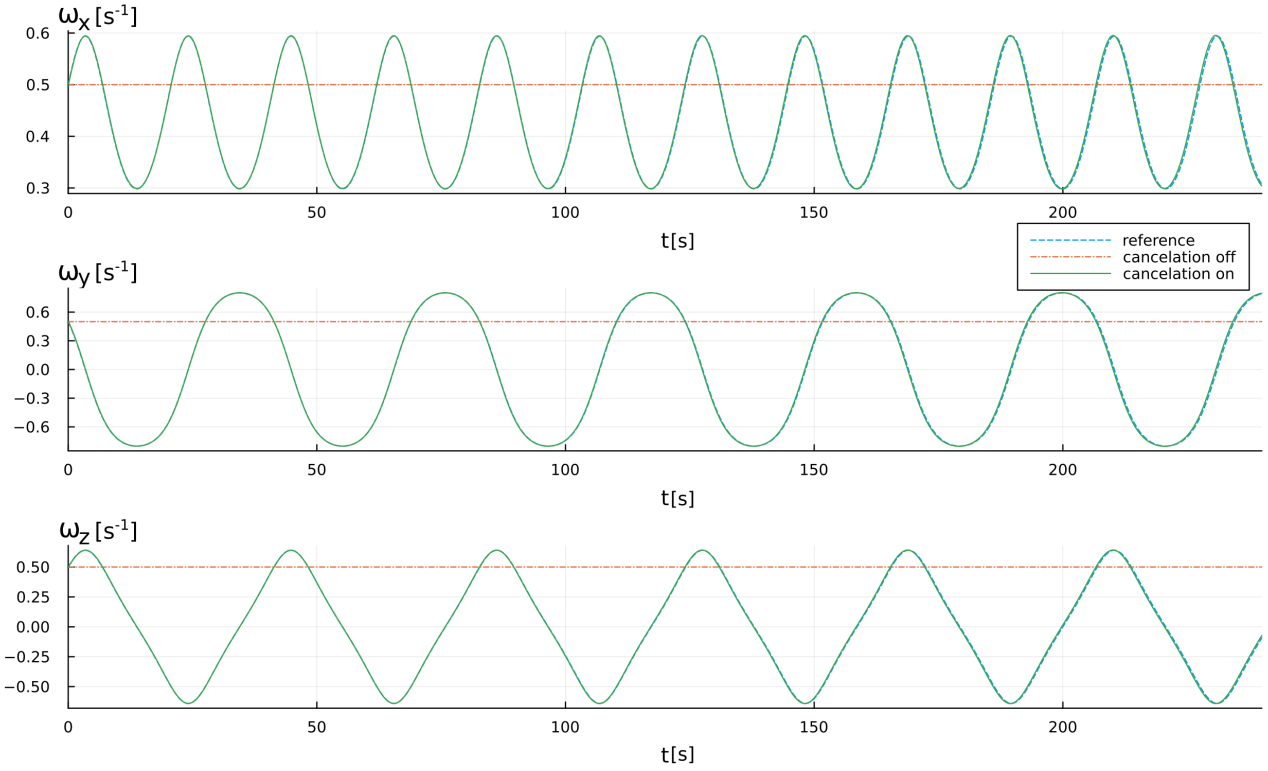

Figure 10: Angular velocity plot of the passive scenario simulation with microsatellite AOCS SUT.

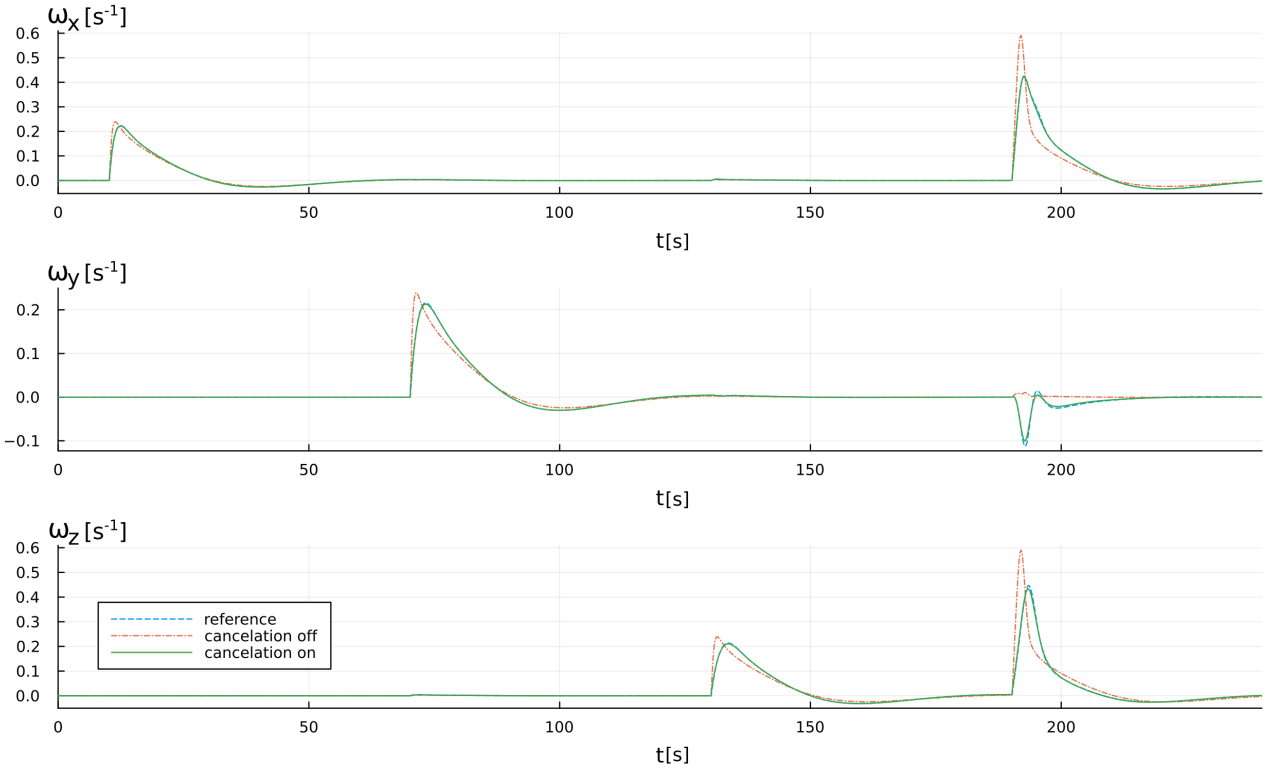

Figure 11: Angular velocity plot of the pointing maneuver scenario simulation with microsatellite AOCS SUT.

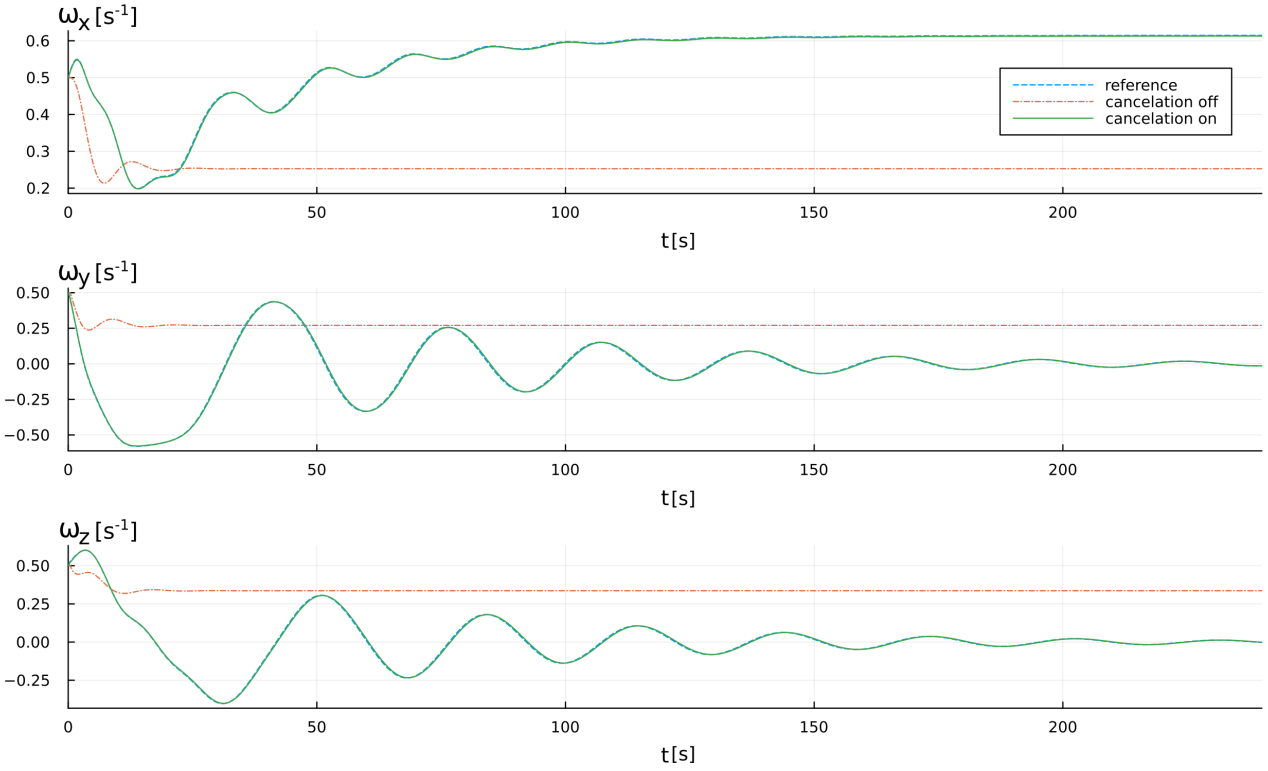

Figure 12: Angular velocity plot of the detumble scenario simulation with microsatellite AOCS.

In summary, the proposed MOI cancellation method corrected the difference in the dynamical response of the SUT in all cases. Moreover, in nearly every case the correction was significantly reducing the difference from the reference run.
The table 1 lists torque maximums generated by the testbed for each simulated case.

	1U CubeSat	3U CubeSat	Microsatellite AOCS
Passive	0.017	0.03	0.16
Pointing	0.008	0.004	0.3
Detumble	0.015	0.025	0.155

Table 1: Maximums of generated torque by the testbed per the SUT and the maneuver.

7 CONCLUSION

The goal of this article was to show, with numerical simulations, the feasibility of building of the testbed for end-to-end AOCS verification and validation with flight ready SUTs. This testbed should be able to include the actuators and the sensors of the SUT in the tested performance, and still provide the dynamical response nearly equivalent to what would be expected in the flight. Specifically, this was to be achieved using a spherical air-bearing platform with external torque generation subsystems. The numerical simulator was developed, modeling several key components of the proposed testbed, including the angular rotation body dynamics with SUT and spherical enclosure, attitude and angular velocity tracking subsystem, torque generation subsystem and a control law for parasitic MOI cancellation. Furthermore, three different SUTs were defined and modeled, together with three different maneuver scenarios. Then, the simulation runs were performed to establish a desired SUT behavior, the behavior of the SUT with the parasitic MOI added and the behavior after the parasitic MOI cancellation.
In all cases, the difference between the reference simulation run and the run without the parasitic MOI cancellation torque is significant enough to alter the angular velocity vector evolution. This shows the effects of affixing the SUT to the spherical enclosure and a problem with the air-bearing testbeds in general. By including the parasitic MOI cancellation torque in the simulations, it was shown that this effect of the added MOI can be removed and the evolution of the angular velocity vector can be driven back to the desired behavior as in the reference run.
The precision and the noise of the attitude and angular velocity tracking subsystem is a possible limitation for the performance, especially for smaller SUTs where the noise effects are more dominant. However, only the basic integration of the sensor readings was used and better performance could be expected with a more advanced filter and sensor fusion techniques. Another way to reduce the noise is by adding more sensors, however, with diminishing returns for each additional sensor. The addition of the absolute tracking with camera and markings on the enclosure can benefit the precision.
The strength of the producible torque by the testbed gives a limitation for larger SUTs. In the table 1, the required maximum torque values show approximately a linear growth with the SUT size. Currently it is unknown what torque maximums are to be realistically expected by the nozzles. In a previous study in [13], a single pressurized air nozzle was able to produce around $5 \times 10^{-4}\,\mathrm{N\,m}$ of torque on a spherical enclosure with radius of $100\,\mathrm{mm}$ and under pressure of $4\,\mathrm{bar}$. That nozzle was manufactured using a 3D printer and was designed for adjustable output direction, sacrificing the torque efficiency. In this study, use of the larger radius spherical enclosures and the greater available area for exerting the pressurized air, as well as possibility to use higher air pressure if more conventional manufacturing processes are used, allow for attaining higher maximum torques per nozzle, as suggested from Eq. 2 and 3. With this in mind, some confidence is to be had for achieving the

necessary torques, at least for middle sized SUTs. The torque output delays and settling time effects posed no problems and the overall controllability was satisfactory.
The PID control law proved to be adequate for every maneuver scenario and SUT. However, it might be worthwhile to explore other controller types which would provide smoother dynamic response, less sensitive to the sensing noise, and remove the need for fine tuning for each SUT. The direct control law did not meet the expectations and was not robust enough to operate in the conditions set within the simulation. Still, the law could be valuable for deriving more advanced control laws.
The main goal of this study, to show the feasibility of parasitic MOI cancellation was achieved, as clearly evidenced by the consistent and significant results presented herein. Building a testbed with such capability has potential to improve the quality and reduce the needed effort for verification and validation of flight ready hardware. This is particularly the case with the nanosatellite class of SUTs. However, the possibility to utilize the testbed for larger satellites was also explored in the article, in the case where only the AOCS subsystem is used and the real MOI of the SUT was simulated with the external torque generation subsystem. This further extends the usability of the testbed, allowing for realistic AOCS tests in the early satellite design phases. Further research can be done in the capability for dynamic change of the MOI, for simulating of the higher complexity scenarios which can include, for example, deployable panels, tether dynamics and fuel sloshing. Also, the performance of the testbed is dependent on the precise knowledge of the SUTs MOI. Measurement of MOI is not straightforward and often difficult to achieve. This testbed could also be utilized for automated precise MOI measurements and the methods for this should be further explored.

REFERENCES

[1] J. Enders, F. Haise Jr, and J. Useller, "Use of aircraft for zero-gravity environment," Tech. Rep., 1966.

[2] H. Handroos and M. Vilenius, "Flexible semi-empirical models for hydraulic flow control valves," 1991.

[3] E. Hairer, S. P. Nørsett, and G. Wanner, *Solving ordinary differential equations. 1, Nonstiff problems*. Springer-Vlg, 1993.

[4] N. Vaughan and J. Gamble, "The modeling and simulation of a proportional solenoid valve," 1996.

[5] J. L. Schwartz, M. A. Peck, and C. D. Hall, "Historical review of air-bearing spacecraft simulators," *Journal of Guidance, Control, and Dynamics*, vol. 26, no. 4, pp. 513–522, 2003.

[6] J. de Lafontaine, J. Côté, J. Naudet, A. Kron, and S. Santandrea, "Proba-2: Aocs software validation process and critical results," in *Proceedings of the 7th International ESA Conference on Guidance, Navigation & Control Systems, Tralee*, County Kerry, Ireland, 2008, pp. 2–5.

[7] *Adns-6010 laser mouse sensor data sheet*, ADNS-6010, AV02-1410EN, Avago technologies, Dec. 2009.

[8] H. Selig, H. Dittus, and C. Lämmerzahl, "Drop tower microgravity improvement towards the nano-g level for the microscope payload tests," *Microgravity Science and Technology*, vol. 22, pp. 539–549, 2010.

[9] M. Kumagai and R. L. Hollis, "Development of a three-dimensional ball rotation sensing system using optical mouse sensors," in *2011 IEEE International Conference on Robotics and Automation*, IEEE, 2011, pp. 5038–5043.

[10] A. Wiegand and S. Weikert, "Concept and performance simulation with astos," in *Proceedings of the SESP 2012: Simulation and EGSE for Space Programmes*, 2012, pp. 1–8.

[11] F. Cacciatore *et al.*, "Rapid deployment of design environment for euclid aocs design," in *6th International Conference on Astrodynamics Tools and Techniques, Darmstadt, Germany*, 2016.

[12] C. Rackauckas and Q. Nie, "Differentialequations. jl–a performant and feature-rich ecosystem for solving differential equations in julia," *Journal of open research software*, vol. 5, no. 1, 2017.

[13] N. Jovanovic, J. M. Pearce, and J. Praks, "Design and testing of a low-cost, open source, 3-d printed air-bearing-based attitude simulator for cubesat satellites," *Journal of Small Satellites*, vol. 8, no. 2, pp. 859–880, 2019.

[14] H. Kolvenbach and M. Voellmy, "Design of a low-cost, spherical air-bearing satellite simulator," in *Symposium on Advanced Space Technologies in Robotics and Automation (ASTRA)*, 2019.

[15] R. C. da Silva, R. A. Borges, S. Battistini, and C. Cappelletti, "A review of balancing methods for satellite simulators," *Acta Astronautica*, vol. 187, pp. 537–545, 2021.

[16] R. Yeşilay, A. Ankaralı, and M. A. Afşar, "A review paper: The dynamics, kinematics, design and control of satellite simulators with spherical air bearing," in *Global Conference on Engineering Research*, 2021.